Energy-Level Effects on the Deformation Mechanism in Microscale Laser Peen Forming

Youneng Wang, Yajun Fan, Sinisa Vukelic, and **Y. Lawrence Yao,** Dept. of Mechanical Engineering, Columbia University, New York, New York, USA

Abstract

Laser microscale peen forming has recently received more and more attention as a viable laser processing technology as it not only imparts desirable residual stress for improvement of fatigue life of the material, but can also precisely control part deformation. In the present study, the effect of energy level on the deformation mechanism in laser microscale peen forming was investigated by both numerical and experimental methods. Deformation curvatures and residual stress distributions of both sides of the specimen, characterized by X-ray microdiffraction, were compared with the results obtained from FEM simulation. The forming mechanism for convex and concave bending was explained in terms of the resulting pressure, compressive stress distribution, and plastic strain. Differences in residual stress distribution patterns were also investigated as a function of the forming mechanism.

Keywords: *Laser Microscale Peen Forming, X-Ray Microdiffraction, Forming Mechanism*

Introduction

Laser forming, usually indicating laser thermal forming, is a flexible rapid prototyping and low-volume manufacturing process that uses laser-induced thermal distortion to shape sheet metal parts without tooling or external forces. Laser forming is well understood both from theoretical and experimental investigations (Vollertsen 1994; Li and Yao 2001). Compared with conventional forming technologies, laser forming has advantages including design flexibility, production of complex shapes, forming of thick plates, and possibility of rapid prototyping. One difficulty, however, is maintaining desirable material properties of metallic parts. This is due to thermal effects that result in undesirable microstructure changes, including recrystallization and phase transformation even without the presence of melting involved (Fan et al. 2005). Also, laser thermal forming may melt or burn the surface and even result in small cracks on the surface.

Laser peen forming (LPF, also known as laser shock forming), developed from laser shock peening technology (Clauer and Holbrook 1981; Chen, Yao, and Kysar 2004), is a purely mechanical forming method achieved through the use of laser energy to modify a target curvature. It has the advantages of laser thermal forming, such as noncontact, tool-less, and high efficiency and precision. Also, its nonthermal nature makes it possible to maintain material properties or even improve them by inducing compressive stress over the target surface. This is desirable in industry as it is important for shaped metal parts to resist cracks due to corrosion and fatigue. In addition, such a compressive stress will generate a strain of the top layer of metal and produce a curvature (Hackel and Harris 2002; Hackel, Halpin, and Harris 2003). Hackel et al. demonstrated that the part can be precisely contoured over its large area by systematically applying impulses inducing local stresses and showed that an enhanced curvature can be achieved if a part is preloaded in a local area by a stress that is near to but below the yielding limit. Meanwhile, Zhou, Zhang, and Cai (2002, 2003) showed the potential of laser peen forming for becoming a flexible manufacturing process with desirable properties as well as the potential for rapid prototyping. They provided insight on deformation mechanisms, mechanical response, and failure behavior for materials under this process. Ji et al. (2004) studied effects of some influence factors, such as the change of laser energy and laser beam diameter, with experimental and numerical methods. Despite the recent advances, the process has still not been fully characterized due to its complex underlying mechanisms for deformation.

In the last 10 years, miniaturization technologies have required new techniques varying from conventional ones like machining to manufacture more complex miniaturized devices, such as using a microforming process (Geiger et al. 2001; Cao et al. 2004). Laser microforming as a new technology has been successfully employed in a number of high-precision industrial applications, such as laser microbending of magnetic disk-drive components and adjustment of contact springs of miniature relays and reed-contacts, etc. (Otsu, Wada, and Osakada 2001; Esser, Schmidt, and Dirscherl 2003). It can be seen that the applications described above all encounter cyclic loadings. These serve as the driving force for the investigation of microscale laser peen forming as a potential method of microforming due to the inherent advantages of laser shock peening (LSP). There currently exists a great deal of work (Zhang and Yao 2002; Chen, Yao, and Kysar 2004) demonstrating that μLSP produces local compressive stress near the surface, thus improving fatigue life of the target. Therefore, it is possible to employ microscale laser peen forming (μLPF) to manufacture complex miniaturized devices as well as improve fatigue life.

This paper studies microscale laser peen forming using both numerical and experimental methods. The effects of laser energies and thickness on the deformation mechanism were investigated experimentally, and experimental data obtained were then used to validate the corresponding simulation model. The sample curvatures before and after laser microscale peen forming were measured using a profilometer to find the net bending effect. Also, both residual stress distributions on the top and bottom surfaces were measured using X-ray microdiffraction. In addition, phenomena about concave and convex bending that result in different patterns of residual stress distribution along the sample's surface were explored. The numerical simulation verified from the experimental results can be used to predict the deformation and further understand the forming mechanism. Hence, the presented work lays some foundation for understanding the process of microscale laser peen forming.

Process of Microscale Peen Forming and Experiment Conditions

Principles of Microscale Laser Peen Forming

When a metallic target is irradiated by an intense (>1 GW/cm^2) laser pulse, the surface layer instantaneously vaporizes into a hot and high-pressure (1~10 GPa) plasma. This pressure may be employed to precisely shape structural components at a microscale resolution in μLPF. Like μLSP, LPF applies a short, intense laser pulse using a micron-sized beam to treat the metallic target surface, and compressive stress is then imparted on the treated surface with micron-level spatial resolution without introducing any thermal effects. For μLSP, the target is placed on a rigid substrate to prevent any movement of the bottom surface. Thus, the resulting compressive residual stress is maximized on the surface and plastic strain is mainly imparted on the top surface. However, the bottom of the target is not restricted for μLPF with two ends clamped by two metal sheets. Typically, the target is much thinner than that of μLSP. Hence, plastic strain may be induced in both sides, and the resulting compressive stress on the treated surface will cause that surface to expand, and thus plastically curve the metal. The curved shape may be convex or concave depending on process parameters. In addition, the surfaces of both sides may be left in a compressive state of stress, which is highly desirable for fatigue and corrosion resistance.

Physical Explanation

μLPF is a purely mechanical process, which imparts compressive stress through a compressive shock wave on the surface of the metal to deform the target. When the laser pulse ablates the coating, the material area beneath the ablating coating undergoes local plastic deformation, which can result in either concave or convex curvature. It can be imagined that the specimen under loading will bend downward first under the downward loading if thickness is thin enough. This downward trend continues during relaxing until other sources overcome this downward inertia. In addition, the stress distribution in the lateral direction is tensile on the bottom side to balance the top's compressive stress, so that this downward bending reinforces plastic deformation on the bottom side because it stretches the bottom. After the inertia disappears, reverse bending follow. This phenomenon may be determined by three sources: the downward loading (inertia after the loading), bending moment, and induced compressive stress. These sources function together to determine the bending. During the loading, the pressure resulting from the laser ablation is the dominant source, which consequently induces the other two sources. Because the loading direction is

downward and the sample is free on the bottom side, the bend is downward in the loading stage. Meanwhile, the induced compressive stress on the top surface elongates the top layer, which leads the strip to bend upward. In addition, the bending angle results in an opposite bending moment and exerts bulging to the specimen, too.

During unloading, the downward inertia makes the specimen bend downward continuously until the other two sources exceed the effect of the downward inertia. Then, the forming direction of the specimen is reversed when the compressive stress becomes dominant. Thus, the phenomenon that the concave or convex final shape occurs is dependent on the effects of these three sources.

Experiment Conditions and Sample Preparation

A frequency-tripled Q-switched Nd:YAG laser (λ=355 nm) in TEM_{00} mode was used in µLPF, and the parameters of pulse duration, wavelength, and beam diameter are shown in *Figure 1*. A line of µLSP shocks was created on the sample surface with a 25 µm spacing. Pulse energies, 202 µJ and 280 µJ, corresponding to laser intensities of 3.57 and 4.95 GW/cm^2, respectively, were applied. A thin layer of high vacuum grease (about 10 microns thick) was spread evenly on the sample surface, and a 16 µm thick polycrystalline aluminum foil, chosen for its relatively low threshold of vaporization, was tightly pressed onto the grease. The sample was placed in a shallow container filled with distilled water around 1 mm above the sample's top surface. The induced deformation is due to shock pressure and not due to thermal effects because only the coating is vaporized during the process.

To investigate the thickness effect under the same laser energy, the samples of copper foils with 100 µm and 200 µm thickness have been chosen. Due to their strong (001) texture, as shown in *Figure 2*, they can be treated as a single crystal in microdiffraction measurements (Chen, Yao, and Kysar 2004). The samples were heat treated to release stress with the temperature of 150°C and duration of one hour. After heat treatment, the texture was measured again by using the conventional X-ray and was found that the stress relief process has almost no effect on texture. The samples were cut to the dimension of 20 mm × 3 mm using a wire EDM and mounted to holders as shown in *Figure 1*, ensuring the specimens are as flat as possible. Before the shocking process, pre-
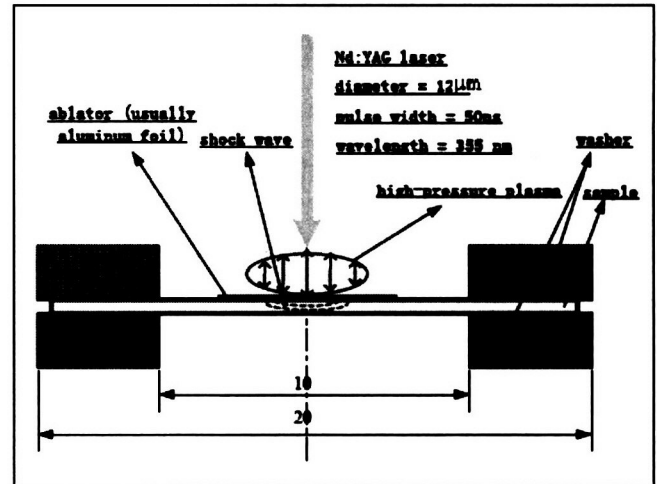

Figure 1
Sample Geometry and Laser Shock Forming Condition (width of sample is 3 mm and screws are used to hold the two washers)
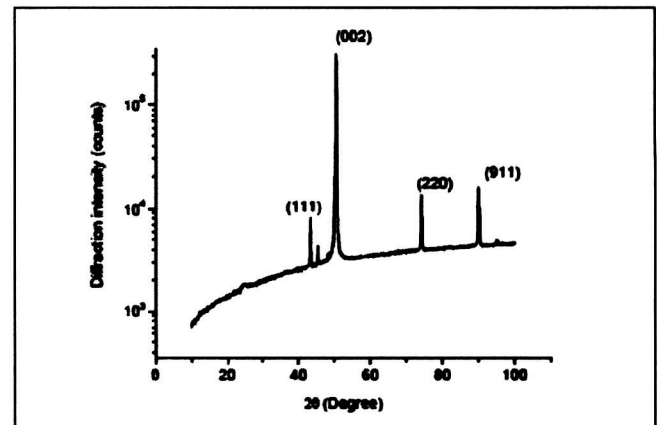

Figure 2
Texture of Annealed 100 µm Copper Sample by Conventional X-Ray

bending was measured by using a Mitutoyo SJ-201P profilometer as shown in *Figure 3*, and the samples with a pre-bending less than 8 µm were chosen for treatment so as to minimize the pre-bending effects.

Post Peen Forming Material Characterization

In this section, the samples after µLPF have been analyzed in terms of global deformation profile and residual stress distribution because these are the most important issues in the area of laser peen forming.

Global Deformation Measurement Using Profilometer

After LPF, the samples' profiles were measured using Surftest SJ-201P of Mitutoyo. The measuring
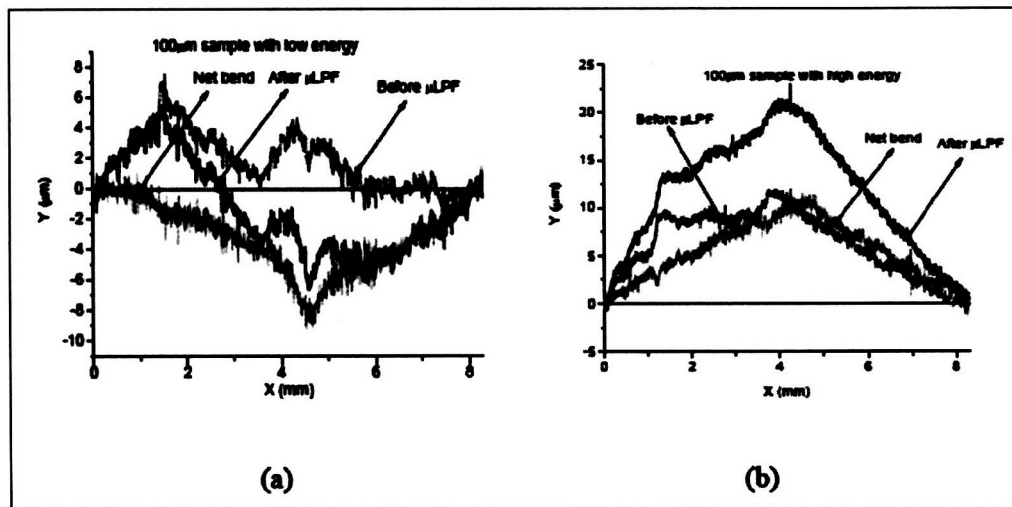
Figure 3
Curvature Measurement on Bottom Side Before and After Peen Forming: (a) 100 μm sample with
3.57 GW/cm² laser intensity; (b) 100 μm sample with 4.95 GW/cm² laser intensity

range is 350 μm with a resolution of 0.4 μm. The measuring force is 4 mN, which assures the detector has no bending effect on the samples while measuring. During the measurement, only the bottom side was measured due to the coating on the top surface. The measured results were shown in *Figure 3*. It can be seen that the bend is downward 8 μm for the 100 μm sample with laser intensity 3.57 GW/cm²; that is, a concave surface was left on curving. For the 100 μm sample with laser intensity 4.95 GW/cm², the bend was upward 10 μm; that is, a convex surface was left on curving. Also, from *Figure 3*, it can be calculated that the bending angle is about 0.11° and 0.14° for these two energy levels, respectively. Thus, μLPF is capable of producing plastic deformation at microscale resolution.

Residual Stress Distribution by X-Ray Microdiffraction

X-ray beam from synchrotron radiation sources (from beamline X20A at National Synchrotron Light Source at Brookhaven National Lab) was used in this study as the extreme intensities allow a short sampling time, and further, the X-ray can be focused by a tapered glass capillary to spot sizes as small as 3 μm. The spot size can be larger than 3 μm because the X-ray beam is divergent. The average grain size of the samples is about 8 μm from both scanning electron microscopy (SEM) and electron backscatter diffraction (EBSD) measurements. In the paper, the X-ray spot size around 15 μm on the sample surface, cover-

ing at least two grains, was used to collect diffraction at each measuring point. Complete details of the X-ray microdiffraction experiment and the corresponding evaluation method of subprofile analysis can be found in Chen, Yao, and Kysar (2004). Because the copper samples used had a very strong texture in the (001) orientation, the (002) reflections were chosen for the X-ray diffraction measurement because the diffraction structure factor for (001) is zero and the reflections are absent (Cullity 1978). To spatially resolve the residual stress induced by μLPF, measurements were made on both top and bottom surfaces across the peened line. The spacing between adjacent measurement points is 10 μm, and the corresponding X-ray diffraction profile at each position is recorded and repeated for each scan line. *Figure 4* shows the typical diffraction profiles corresponding to the 100 μm sample under laser energy of 3.57 GW/cm². It can be seen that the profiles close to the peened line center are broadening and the peaks are shifted. As a result, the broadening and shift of the profile can be interpreted in terms of the residual stress state.

After obtaining the X-ray diffraction profiles at different positions in the peened region, the lateral residual stress on the sample surface can be estimated using the subprofile method of Chen, Yao, and Kysar (2004). The spatial distribution across the peened region was plotted as in *Figure 5*. For the 100 μm sample under 3.57 GW/cm² laser intensity, a compressive residual stress is generated near the center of the peened region and bordered by a region of tensile stress on the bottom side. For the top surface, there is a tensile residual stress near the center and is bordered by a region of compressive stresses. For the 100 μm sample under 4.95 GW/cm², a compressive residual stress is generated on the bottom side, and there is a tensile residual stress on the top surface. Although the laser spot size is only 12 μm, the high shock pressure in μLPF can generate significant compressive residual stresses over a much larger

4

Figure 4
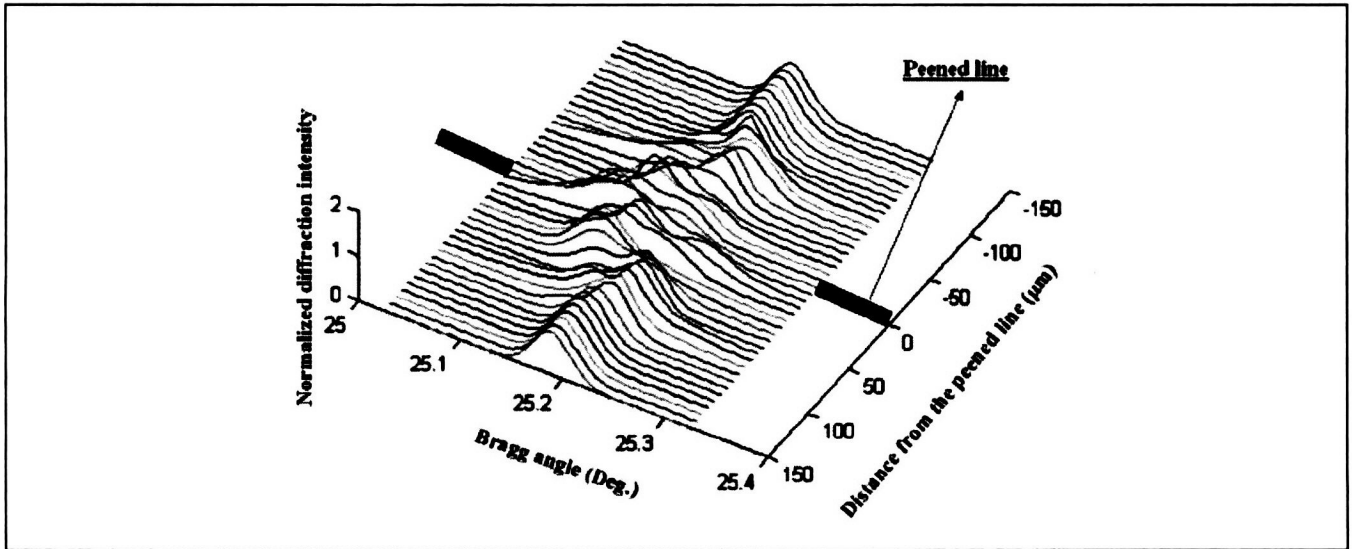**Typical 3-D X-Ray Profile Spatial Distribution Across Shock Line of 100 μm Sample on Bottom Side**
(laser energy 3.57 GW/cm² , spatial resolution 10 μm from line)

(a)

(b)

(c)

(d)

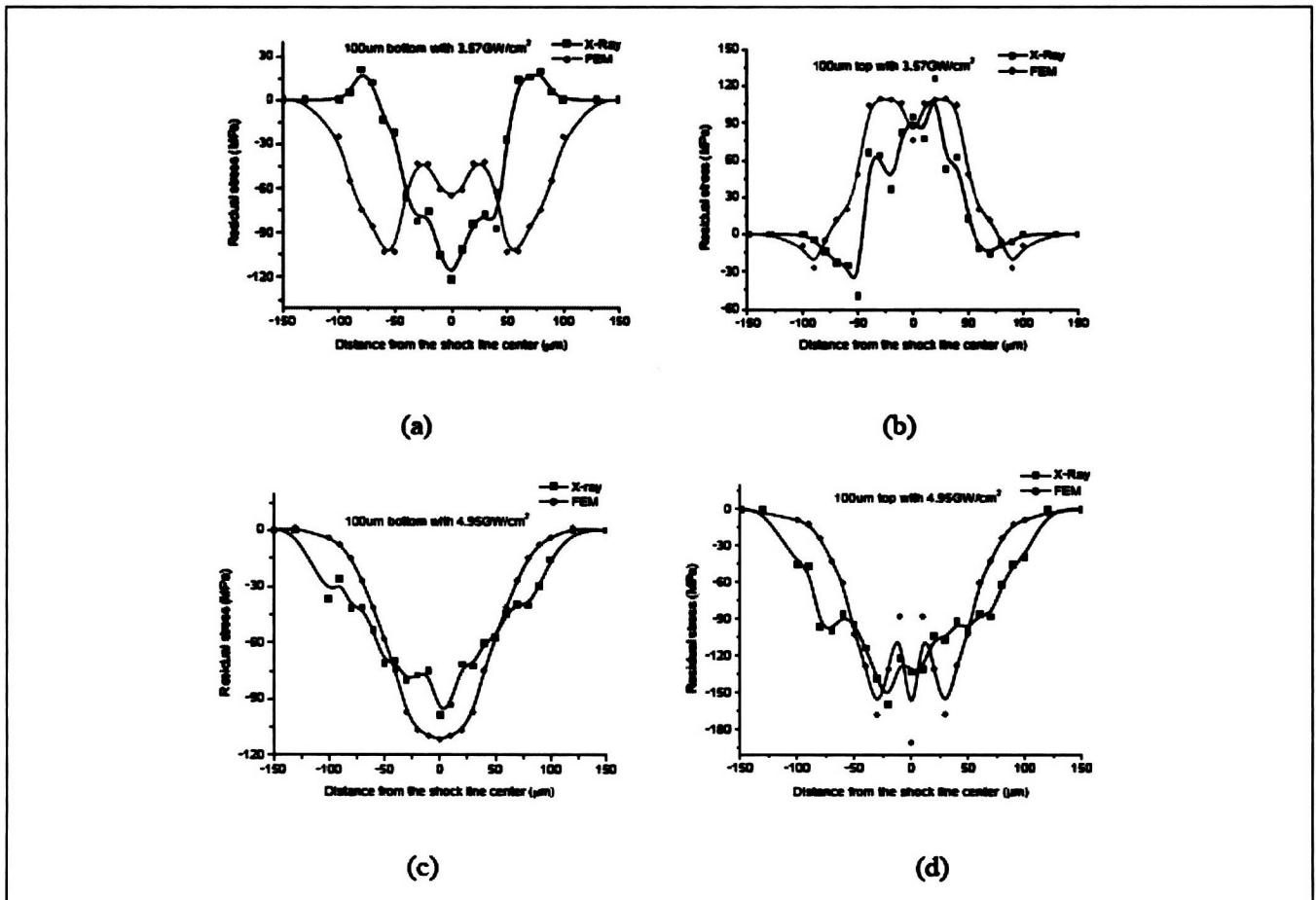***Figure 5***
Residual Stress Distribution by X-Ray Microdiffraction and FEM Simulation: (a) 100 μm sample bottom with 3.57 GW/cm² laser
intensity; (b) 100 μm sample top with 3.57 GW/cm² laser intensity; (c) 100 μm sample bottom with 4.95 GW/cm² laser intensity;
(d) 100 μm sample top with 4.95 GW/cm² laser intensity

5

region of up to 200 μm. For the 4.95 GW/cm^2 condition, the induced compressive stress is also larger than that of 3.57 GW/cm^2. The compressive stress is estimated to have a maximum value of –150 MPa near the center and cover a region of 120 μm in width on the surface from the center for the 4.95 GW/cm^2 laser intensity. It can be seen that compressive residual stresses are induced in both sides for the convex bending, where the top side is tensile and the bottom side is compressive for concave bending.

FEM Simulation

Shock Pressure and Hardening and Strain Rate Effects

For this numerical simulation, the laser forming process is modeled as purely mechanical. The analytical shock model is assumed the same as that of μLSP and follows Fabbro et al.'s model (1990), which assumes that the laser irradiation is uniform and shock propagation in the confining medium is one-dimensional. The shock pressure induced in a confined region is given by the following relationship (Fabbro et al. 1990):

$$\frac{dL(t)}{dt} = \frac{2P(t)}{Z} \qquad (1)$$

$$\left(\frac{Z}{2} + \frac{3}{4\alpha}\right)\left(\frac{dL(t)}{dt}\right)^2 + \frac{3Z}{4\alpha}L(t)\frac{d^2L(t)}{dt^2} = AI(t) \qquad (2)$$

where $Z = 2/(1/Z_1 + 1/Z_2)$ is the shock wave impedance; the subscripts, 1 and 2, denote the solid target material and the confining medium, respectively; $L(t)$, $P(t)$, A, and α are plasma thickness, shock pressure, absorption coefficient, and interaction coefficient, respectively. To account for the small laser spot size, the spatially uniform shock pressure, $P(t)$, relates to the spatially nonuniform shock pressure as $P(r,t) = P(t)\exp(-r^2/2r_0^2)$, where r is the radial distance from the center of the laser beam and r_0 the radius of laser beam, which is 6 μm in this paper. The complete detail of the application of Fabbro's model (1990) for μLSP can be found in Zhang and Yao (2002).

In LPF, the target is subjected to a very strong shock pressure (>1 GPa), a very short interaction time (<100 ns), and very high strain rate (>100,000 s^{-1}). The increased strain rate has a much greater effect on the material flow stress in LPF than a static loading, which in turn influences the deformation of

the material. The total strain rate during laser forming can be decomposed into $\dot{\varepsilon}_{ij} = \dot{\varepsilon}_{ij}^e + \dot{\varepsilon}_{ij}^p$, where $\dot{\varepsilon}_{ij}$, $\dot{\varepsilon}_{ij}^e$, and $\dot{\varepsilon}_{ij}^p$ represent total strain rate, elastic strain rate, and plastic strain rate, respectively. The relation between strain, ε_{ij}^p, stress, σ_{ij}, under plastic deformation can be written as

$$d\varepsilon_{ij}^p = (d\lambda)\frac{df}{d\sigma_{ij}} \qquad (3)$$

where f is the flow potential and $d\lambda$ is a constant. When the von Mises criterion is applied for f, the above equation takes the following form for $d\varepsilon_{11}$:

$$d\varepsilon_{11}^p =$$
$$d\lambda \frac{\partial}{\partial\sigma_{11}}\left\{\frac{1}{6}\left[(\sigma_{11}-\sigma_{22})^2 + (\sigma_{11}-\sigma_{22})^2 + (\sigma_{11}-\sigma_{22})^2\right] + \sigma_{12}^2 + \sigma_{13}^2 + \sigma_{23}^2\right\} \qquad (4)$$
$$= (d\lambda)S_{11}$$

where S_{ij} is the deviatoric part of stress.

In the numerical simulation, the isotropic hardening is accounted for by a Johnson-Cook plasticity law, which takes both strain and strain rate effects into consideration. Based on the Johnson-Cook model, the yield strength is written as:

$$Y = Y_0\left[1 + C\ln\frac{\dot{\varepsilon}}{\dot{\varepsilon}_0}\right][1 + B\varepsilon]^n\left(1 - \frac{T-T_0}{T_m-T_0}\right) \qquad (5)$$

where C is the logarithmic rate sensitivity, ε is strain, $\dot{\varepsilon}$ is strain rate, and B and n are material parameters describing work-hardening effects. In this paper, the temperature effect is negligible because there is no thermal effect in LPF.

Simulation Conditions

In the simulation, a two-dimensional deformation state was assumed. This is reasonable because μLSP results in a two-dimensional deformation if shocking the sample under the conditions as described in an earlier section (Chen, Yao, and Kysar 2004). A length of 10 mm is computed, and bias mesh in the lateral direction is applied with the finest mesh in the middle as small as 2.3 μm, which is much smaller than the laser beam of 12 μm. The mesh in the depth direction is constant with a size of 2 μm. CPE4R elements were employed in the analysis. Also, the two ends of the sample are fixed in the simulation, and the bottom and top sides are free.

6

The finite element solvers ABAQUS/Explicit and ABAQUS/Standard were combined to perform the simulation. These two solvers accomplish different calculations during this simulation. The simulation is divided into two steps: (1) a high dynamic laser shock loading with the explicit version and (2) static unloading corresponding to the relaxation process with the implicit version. After the ABAQUS/Explicit analysis finishes, the information including the stress, strain, and displacement was exported to the ABAQUS/Standard analysis. The ABAQUS/Explicit module is a nonlinear, explicit, time-integration finite element code that is especially well suited for solving high-speed, short-duration, highly dynamic events that require many small time step increments to obtain a high-

resolution solution. One important issue about the modeling is the balance between a short time for dynamic shock-solid interaction (2~3 times of the laser pulse duration) and a much longer relaxation time (up to 1 second) to reach a stabilized mechanical state.

Simulation Model Validation

In *Figure 6a*, the calculated residual stress field near the laser shocked region of the 100 μm sample with 3.57 GW/cm^2 is shown. The residual stress contour of the whole computed length indicates that the bend is downward. This trend is the same as that of the experimental result shown in *Figure 3a*. The simulation result for the 100 μm sample with high energy is shown in *Figure 6b*, whose bending direction is con-
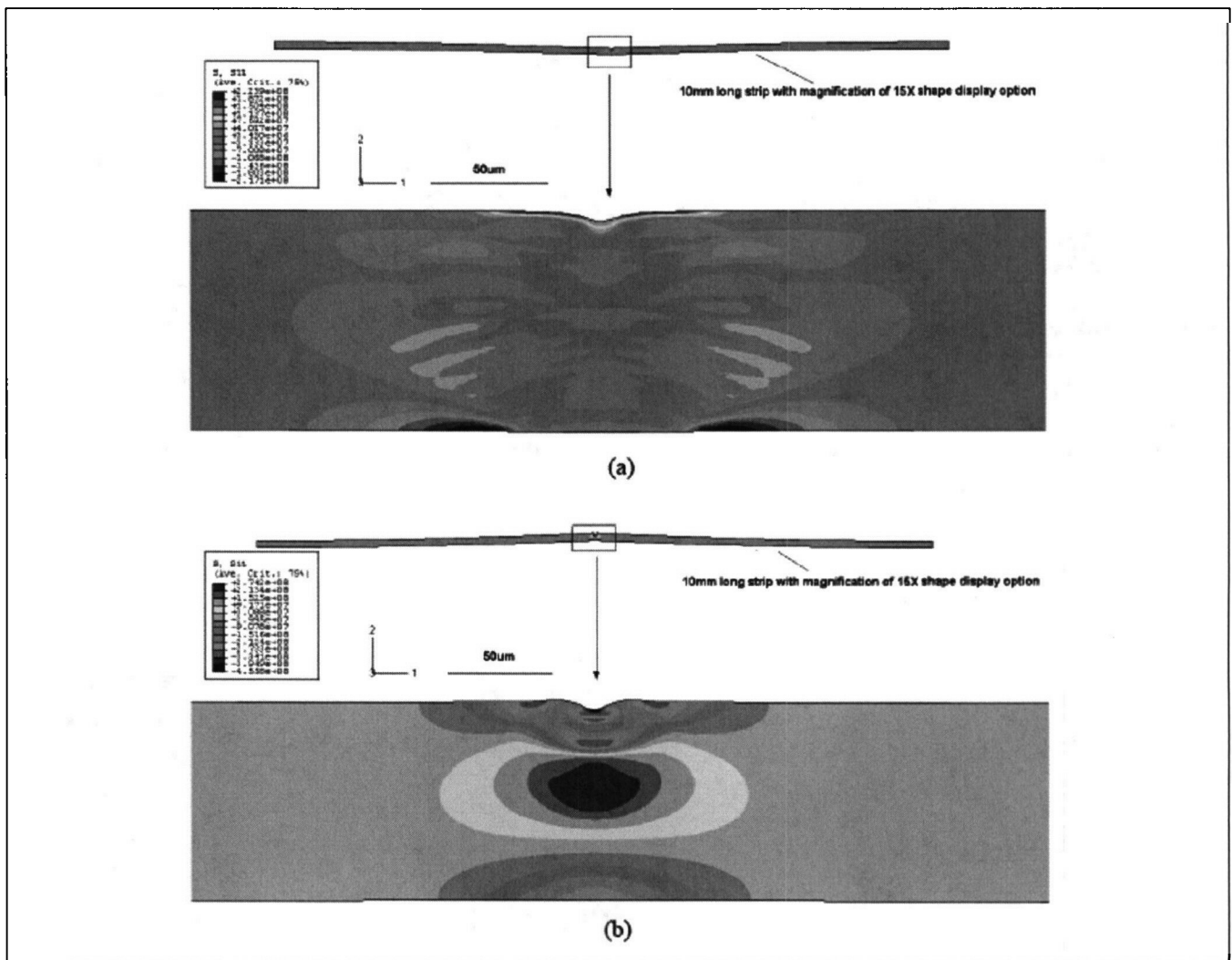
Figure 6
Residual Stress Contour After Peen Forming by FEM Simulation for 100 μm Samples: (a) 3.57 GW/cm^2 laser intensity; (b) 4.95 GW/cm^2 laser intensity

7

sistent with the experiment result from the profilometer (*Figure 3b*). For the residual stress distribution, it is found from *Figure 6* that the simulation model gives almost the same patterns as the experiment results; that is, the top side is mainly tensile stress, while the bottom side is compressive for the 3.57 GW/cm^2 case, and both sides are compressive for the 4.95 GW/cm^2 case. To compare the simulation results of residual stress with the experimental results, the corresponding residual stress of the simulation at each point was obtained by averaging over the effective penetration depth of X-ray microdiffraction. If it is chosen that surface layer contributes 95 percent of total diffracted intensity, the X-ray penetration depth for copper specimen can be calculated as:

$$x = \frac{K_x \times \sin \theta_0}{2\mu} \qquad (6)$$

where θ_0 is the ideal Bragg angle, μ is the linear absorption coefficient, and $K_x = \ln[1/(1-0.95)]$. The effective depth is approximately 15 μm for the copper (Cullity 1978). In this surface layer of depth 15 μm, the averaged stresses at each point with respect to X-ray measurement points were obtained and are shown in *Figure 5*. It can be seen that the simulation results show similar patterns and generally agree with the experimental results. *Figure 7* shows the comparison of the curvature on the bottom side after peen forming for the simulation and experiment. The simulated profiles agree well with the experimental results from profilometer as well as the overall deformation depth. These general agreements for residual stress distribu-

tion and deformation are indicative of the model's validity. Thus, the model can be used to predict the response to μLPF for different process parameters.

Further Investigations of Distinctive Forming Mechanisms

Plastic Strain Distribution

As seen from *Figure 8a*, the resulting displacements of the loading step for two energy levels are very close, that is, –2 μm for low energy and –3 μm for high energy, but the displacement after unloading for 3.57 GW/cm^2 reaches –12 μm, while that of 4.95 GW/cm^2 is only –6 μm. This downward displacement reinforces the plastic deformation on the bottom side. *Figure 8b* shows the time history of plastic strain in the lateral direction. It can be seen that plastic strain on the bottom side increases along the displacement, while the top side is mainly determined by the period of the shock loading. For 4.95 GW/cm^2, plastic strain on the top side is much larger than that of the bottom side—almost 10 times, but the plastic strains on both sides are almost same for 3.57 GW/cm^2. The difference makes the difficulty of upward bending for the 3.57 GW/cm^2 case but favors upward bending for 4.95 GW/cm^2. Hence, it is easier to induce convex bending with a high laser energy rather than a low energy.

Compressive Stress Distribution

From both experimental and simulation results, it is found that both sides have compressive residual stresses for convex bending, and one side is tensile
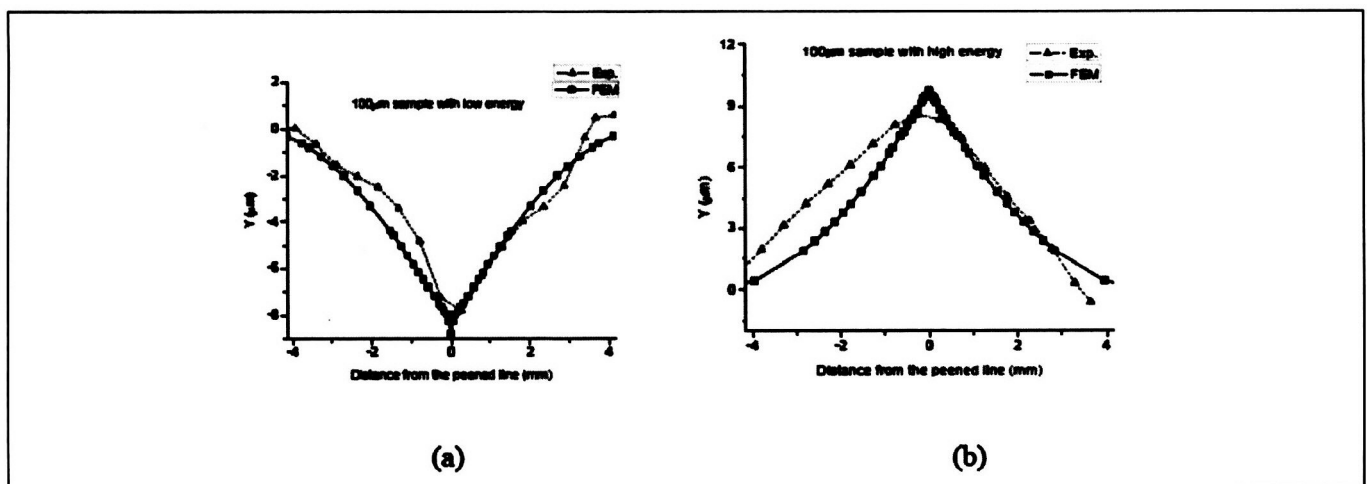

(a)   (b)

Figure 7
Curvature Comparison of FEM and Experimental Results: (a) 100 μm sample with 3.57 GW/cm^2 laser intensity;
(b) 100 μm sample with 4.95 GW/cm^2 laser intensity

8

and the other side is compressive for concave bending. *Figure 9a* gives the time history of stress for the center point on the top surface. It indicates that the stress on the bottom is first tensile to balance the compressive stress of the top surface, and then changes to compressive as the specimen bends upward for the 4.95 GW/cm² laser intensity. For the case of 3.57 GW/cm², the tensile residual stress occurs on the treated surface as the bending is reversed.

Figure 9b shows the distribution of averaged stress within 30 μm from the top right after the moment of unloading for two energy levels. This demonstrates that the range and magnitude of compressive stress induced by 4.95 GW/cm² are much larger than those induced by 3.57 GW/cm². The range of compressive stress for 4.95 GW/cm² is around ±200 μm, while that of 3.57 GW/cm² is only ±100 μm. The effect of bending moment is relatively small compared with that of compressive stress because the bending angle is very small, about 0.1°. Therefore, the induced compressive stress plays a dominant role on the bending after loading. If the compressive stress distribution is wide, it is harder to generate downward bending. So it is more difficult to obtain convex shape for low energy than high energy in terms of compressive stress distribution. Wave propagation of the point 60 μm away from the center on the top surface as shown in *Figure 9c* gives some insight of the difference of compressive stress distribution for these two cases. From *Figure 9c*, the pressure at that point for 4.95 GW/cm² is two and half times

that of the pressure for 3.57 GW/cm². However, shock wave propagation in the depth direction is similar for both cases, as shown in *Figure 9d*. The difference of wave propagation in the depth and surface directions may be due to the material volume that can be compressed. For either case, there is little material that can be compressed in the depth direction because the thickness is too thin, but for the surface direction there is enough material for compressing.

The tension caused by compressive stress in 4.95 GW/cm² case, which exerts bulging in the specimen, will restrain downward bending significantly compared to the 3.57 GW/cm² case. That is why the downward bending of 4.95 GW/cm² is smaller than that of 3.57 GW/cm². After the combined effect of bending moment and compressive stress overcomes the downward effect caused by the inertia, the reverse bending follows. As discussed previously, the reverse magnitude is mostly determined by the induced compressive stress and not by the bending moment. Hence, the reverse magnitude of the 4.95 GW/cm² case is larger than that of the 3.57 GW/cm² case. For the 4.95 GW/cm² case, the compressive stress even overcomes the opposite bending moment and results in upward bending.

Specimen Thickness Effect on Forming

The global deformation and residual stress pattern by μLPF are determined by various parameters, such as laser pulse energy, target material, and thickness of metal sheet. Here, thickness effects are investigated.

(a)   (b)
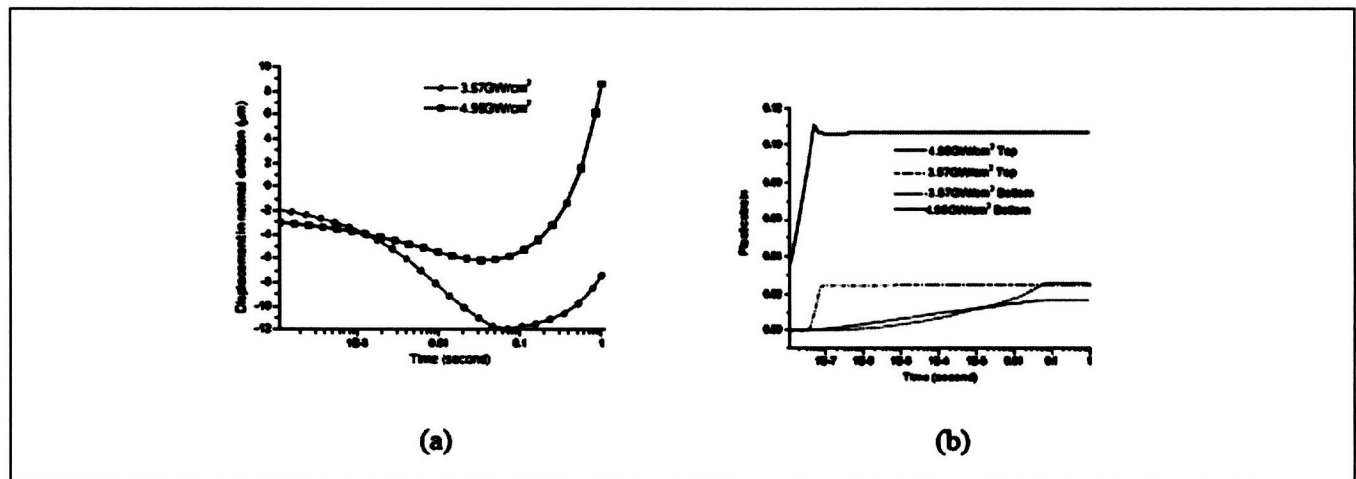
Figure 8
Time Trace by FEM Simulation for 100 μm Samples: (a) normal displacement of center point on bottom surface;
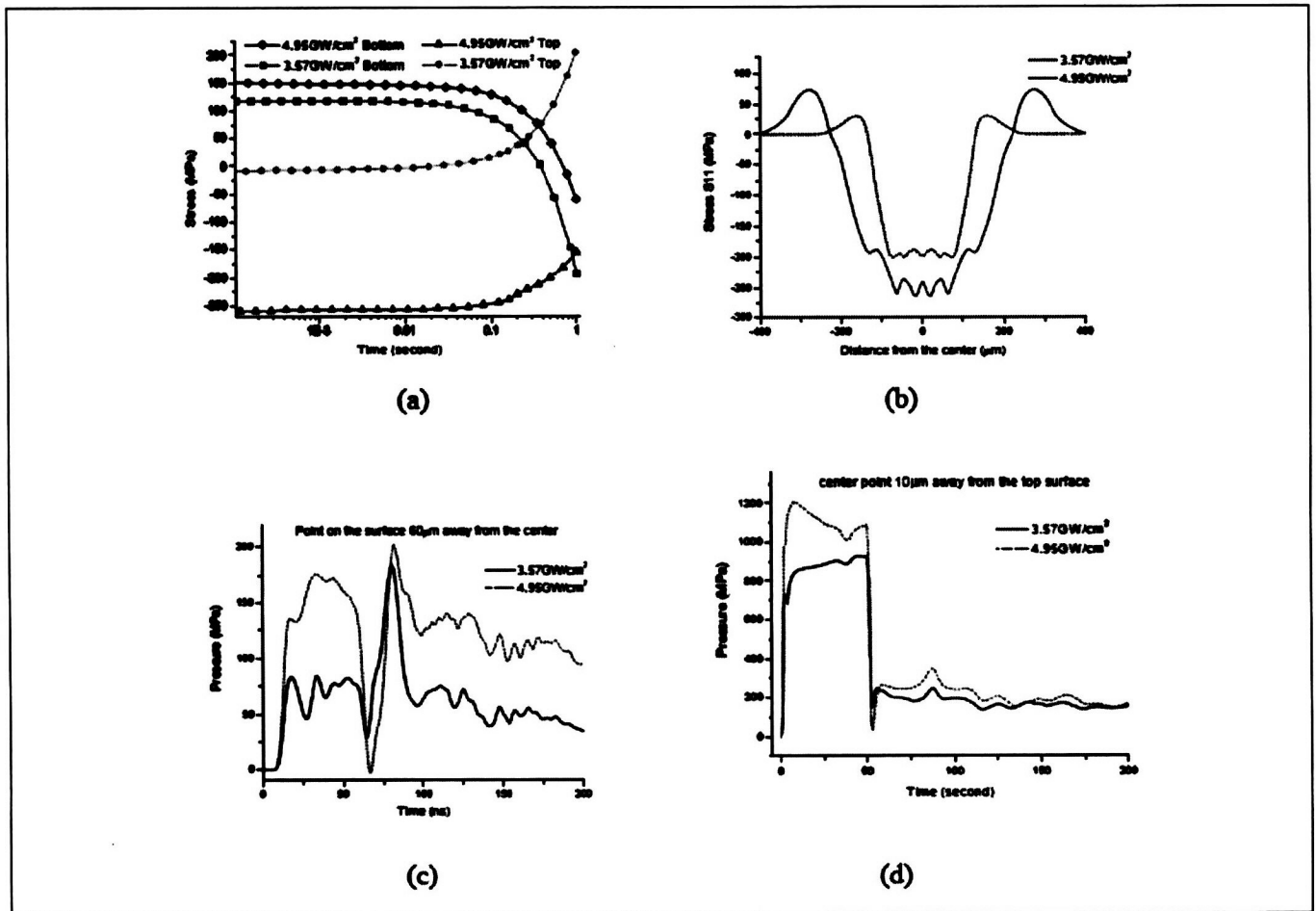(b) plastic strain (along surface direction) of center point for both sides of surface

9

(a)   **(b)**

(c)   **(d)**

Figure 9
Stress and Wave Propagation from FEM: (a) time trace of lateral stress of central points on both sides of surface; (b) spatial distribution of stress on top surface at beginning of unloading; (c) wave propagation along surface direction on top surface; (d) wave propagation in depth direction

Figure 10 gives the global deformation for the 200 μm copper sample by μLPF under the 4.95 GW/cm^2 condition. It is clear that it is convex bending, and the magnitude of the deformation is around 5 μm, corresponding to the bending angle of 0.057°. As seen in *Figure 11*, as thickness increases, the induced compressive stress is almost same as that of 100 μm, and consequently, the global deformation decreases because the moment of inertia increases. In addition, the bending mode is the same as that of 100 μm under the same conditions. Also, the simulation result is comparable with the experimental results shown in *Figure 10*. According to the above results, it may be said that thickness has almost no effect on residual stress distribution. The residual stress distribution by both simulation and experiment is shown in *Figure 11*. Both show the same trend and are comparable. As shown in *Figure 11*, the residual stresses
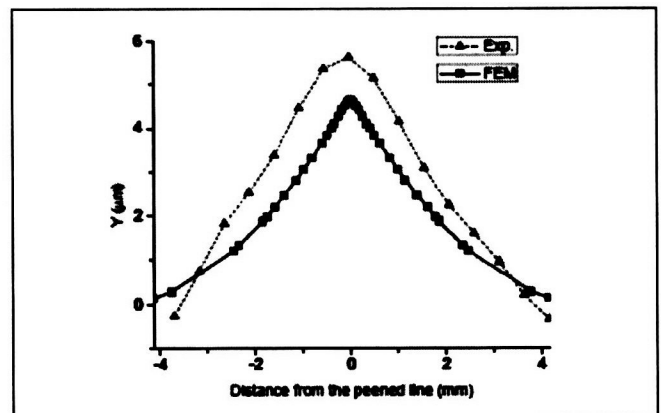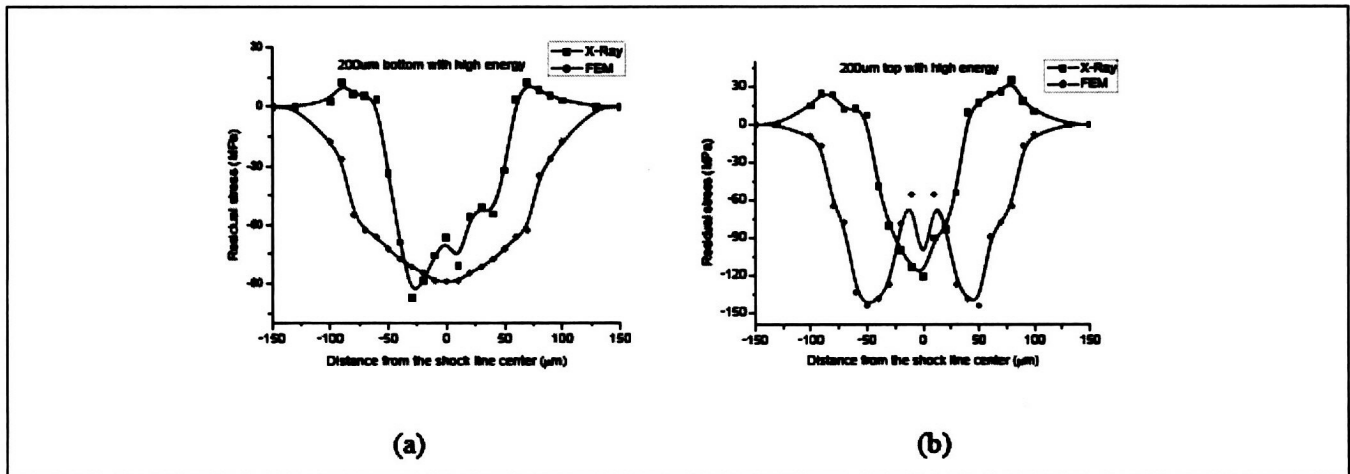

Figure 10
Curvature Resulting from μLPF with Condition of 4.95 GW/cm^2 Laser Intensity for 200 μm Copper Sample

are compressive on both sides, which is similar with those of 100 μm under the same conditions, but the magnitude of the stress is a little smaller than that of
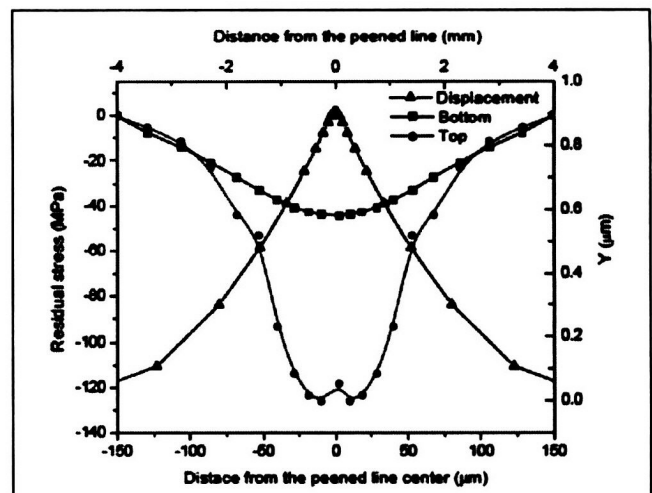
10

Figure 11
Residual Stress Distribution by X-Ray Microdiffraction and FEM Simulation: (a) 200 μm sample bottom with high energy;
(b) 200 μm sample top with high energy

100 μm on both sides. *Figure 12* shows the simulation results for the 200 μm sample under the 3.57 GW/cm² laser intensity. The bending is convex and residual stresses are compressive on both sides, which is in accordance with the forming mechanism discussed previously.

Laser peen forming of thick strips has been investigated by (Hackel and Harris 2002), but there is no concave bending reported. This may be due to the thickness effect because the specimen used in this paper is much thinner than those used by Hackel and Harris (2002), which was several millimeters. Therefore, the downward bending effect caused by impacts (loading) and the followed inertia is very small in Hackel and Harris (2002) because the inertia of moment, which is proportional to the cube of thickness, is big enough to prevent the downward bending. So the convex curving effect is mainly resulting from the surface elongation.

Figure 12
Displacement of Central Point on Bottom and Residual Stress Distributions of Both Sides by FEM Simulation for 200 μm Sample with 3.57 GW/cm²

Comparison with Mechanical Shot Peen Forming

Kondo, Tsuzuki, and Kato (1981) have studied the mechanisms about concave or convex deformation of sheet metals in shot peen forming by using a two-dimensional model. They concluded that when the upper material flow was larger than lower flow, it would result in convex; when the lower material flow was larger, it would result in concave. Kopp and Schulz (2002) pointed out that a concave or convex curvature was determined by the local plastic deformation, too. The laser peen forming has some similarity with shot peen forming. For example, both

are a highly dynamic process and induce compressive stresses into the target. However, the specimen used in this paper is much thinner than those used in shot peen forming, which was several millimeters as in Hackel and Harris (2002). So the downward bending effect caused by impacts and the followed inertia can be ignored in shot peen forming. But in laser peen forming as discussed in this paper, the concave phenomenon exists even when the surface plastic flow is similar to the bottom plastic flow as shown in *Figure 8b* due to the downward effect caused by the downward loading.

11

Conclusions

In this paper, microscale laser peen forming on copper samples of different thickness with two levels of laser energy was investigated by using both experimental and numerical methods. The simulation model was verified by the experimental results measured by a profilometer and X-ray microdiffraction. For 100 μm samples, the bending mode is based on applied laser energy. If the 4.95 GW/cm² laser intensity was applied, the bending is convex and the bending angle is around 0.14°. However, the bending is concave with the bending angle of 0.11° if the 3.57 GW/cm² laser intensity was applied. This deformation phenomenon was explained by using the validated model in terms of the combined effects of three sources: impact (downward loading), induced compressive stress, and bending moment. It was shown that the residual stress patterns are mainly determined by deformation mechanisms. For concave bending, the bottom side is compressive, while the top is tensile. For convex bending, both sides are compressive. In the cases of the 100 μm samples, the maximum compressive stress is –120MPa for laser intensity 3.57 GW/cm² and –160MPa for 4.95 GW/cm² intensity. The effected area for both energy levels is around ±150 μm, which is much larger than that of laser shock peening under the same conditions. In general, the extension of microscale laser shock peening to forming is valuable with respect to the residual stress distribution as well as the capability to deform the target at a microscale resolution.

Acknowledgment

References

Cao, J.; Krishnan, N.; Wang, Z.; Lu, H.; Liu, W.K.; and Swanson, A. (2004). "Microforming: experimental investigation of the extrusion process for micropins and its numerical simulation using RKEM." *ASME Journal of Mfg. Science and Engg.* (v126), pp642-652.

Chen, H.; Yao, Y.L.; and Kysar, J.W. (2004). "Spatially resolved characterization of residual stress induced by micro-scale laser shock peening." *ASME Journal of Mfg. Science and Engg.* (v126, n2), pp226-236.

Clauer, A.H. and Holbrook, J.H. (1981). "Effects of laser induced shock waves on metals." *Shock Waves and High Strain Phenomena in Metals-Concepts and Applications.* New York: Plenum, pp675-702.

Cullity, B.D. (1978). *Elements of X-Ray Diffraction,* 2nd ed. London: Addison-Wesley Publishing Co., Inc., pp268-270.

Esser, G.; Schmidt, M.; and Dirscherl, M. (2003). "Laser adjustable actuators for high-accuracy positioning of micro components." *Proc. of SPIE - The International Society for Optical Engineering* (v5063), 4th Int'l Symp. on Laser Precision Microfabrication, pp177-182.

Fabbro, R.; Fournier, J.; Ballard, P.; Devaux, D.; and Virmont, J. (1990). "Physical study of laser-produced plasma in confined geometry." *Journal of Applied Physics* (v68, n2), pp775-784.

Fan, Y.; Yang, Z.; Cheng, P.; Egland, K.; and Yao, Y.L. (2004). "Effects of phase transformations on laser forming of Ti-6Al-4V alloy." *Transactions of NAMRI/SME* (v33), pp235-242.

Geiger, M.; Kleiner, M.; Eckstein, R.; Tiesler, N.; and Engel, U. (2001). "Microforming." *Annals of the CIRP* (v50, n2), pp445-462.

Hackel, Lloyd and Harris, Fritz (2002). "Contour forming of metals by laser peening." U.S. Patent 6410884.

Hackel, Lloyd A.; Halpin, John M.; and Harris, Fritz B. (2003). "Preloading of components during laser peenforming." U.S. Patent 6670578.

Ji, W.; Zhou, J.; Dai, Y.; and Zhang, Y. (2004). "FEM simulation on the laser shock forming of metal sheet." *Proc. of 6th ICFDM,* Xi'an, China.

Kopp, R. and Schulz, J. (2002). "Flexible sheet forming technology by double sided simultaneous shot peen forming." *Annals of the CIRP* (v51), pp195-198.

Kondo, K.; Tsuzuki, S.; and Kato, A. (1981). "Investigations on peen forming (2nd report: on the forming mechanism)." *Proc. of ICSP-1,* pp565-572.

Li, W. and Yao, Y.L. (2001). "Numerical and experimental investigation of convex laser forming process." *Journal of Manufacturing Processes* (v3, n2), pp73-81.

Otsu, M.; Wada, T.; and Osakada, K. (2001). "Micro-bending of thin spring by laser forming and spark forming." *Annals of the CIRP - Manufacturing Technology* (v50, n1), pp141-144.

Vollertsen, F. (1994). "Mechanisms and models for laser forming." *Laser Assisted Net Shape Engineering, Proc.* of the LANE'94, B. Meisenbach, ed. (v1), pp345-360.

Zhang, W. and Yao, Y.L. (2002). "Micro-scale laser shock processing of metallic components." *ASME Journal of Mfg. Science and Engg.* (v124, n2), pp369-378.

Zhou, M.; Zhang, Y.; and Cai, L. (2002). "Laser shock forming on coated metal sheets characterized by ultrahigh-strain-rate plastic deformation." *Journal of Applied Physics* (v91, n8), pp5501-5503.

Zhou, M.; Zhang, Y.K.; and Cai, L. (2003). "Ultrahigh-strain-rate plastic deformation of a stainless-steel sheet with TiN coatings driven by laser shock waves." *Applied Physics A - Materials Science & Processing* (v77), pp549-554.

Authors' Biographies

Youneng Wang is a PhD candidate at Columbia University. He received his MS in manufacturing engineering from the University of Michigan in 2004. His research interests are laser shock peening and laser micromachining.

Yajun Fan is a PhD candidate in the Dept. of Mechanical Engineering at Columbia University. He received an MS in materials science from Pennsylvania State University in 2003.

Sinisa Vukelic is a PhD candidate in the Dept. of Mechanical Engineering at Columbia University.

Y. Lawrence Yao is a professor at Columbia University. He received his PhD from the University of Wisconsin-Madison in 1988. He is interested in multidisciplinary research in manufacturing and design, nontraditional manufacturing processes, and laser materials processing. He serves on the board of directors of the Laser Institute of America.